

Towards measuring nuclear-spin-dependent and isotopic-chain atomic parity violation in Ytterbium

K. Tsigutkin¹, J. E. Stalnaker^{1a}, D. Budker^{1,2}, S. J. Freedman^{1,2}, and V. V. Yashchuk³

¹ Department of Physics, University of California, Berkeley, CA 94720-7300

² Nuclear Science Division, Lawrence Berkeley National Laboratory, Berkeley CA 94720

³ Advanced Light Source Division, Lawrence Berkeley National Laboratory, Berkeley CA 94720

Received: date / Revised version: date

Abstract. We discuss experiments aimed at measurements of atomic parity nonconservation (PNC) effects in the $6s^2\ ^1S_0 \rightarrow 5d6s\ ^3D_1$ transition (408 nm) in atomic Ytterbium ($Z=70$). According to theoretical predictions, the PNC-induced E1 amplitude of this transition is ~ 100 times larger than the analogous amplitude in Cs. Such an experiment will determine differences in PNC effects between different hyperfine components for odd-neutron-number Yb isotopes and, thereby, will allow measurements of the nuclear anapole moments in nuclei with unpaired neutrons. In addition, measurements of PNC in different isotopes would give information on neutron distributions within the nuclei. The apparatus designed and built for this experiment is described, and results of measurements towards understanding of systematic effects influencing the accuracy, and the current status of the ongoing PNC measurements are presented.

PACS. 32.80.Ys Weak-interaction effects in atoms – 32.70.-n Intensities and shapes of atomic spectral lines – 32.60.+i Zeeman and Stark effects

1 Introduction

Atomic ytterbium (Yb) was proposed as a system for measuring the effects of parity nonconservation (PNC) by D. DeMille [1] who pointed out a rather non-obvious enhancement of the PNC transition amplitude arising due to configuration mixing in addition to relative proximity of the excited $5d6s\ ^3D_1$ and $6s6p\ ^1P_1$ states of opposite nominal parity (Fig. 1). The PNC-induced $6s^2\ ^1S_0 \rightarrow 5d6s\ ^3D_1$ transition amplitude has been calculated [1,2,3] to be two orders of magnitude larger than the PNC amplitude in cesium where high-precision measurements have been carried out [4,5].

While the accuracy of the theoretical calculations of PNC effects in Yb is at a $\sim 20\%$ level [2,3], there is little hope that it will ever reach sub-one-percent levels achieved for Cs and other single-electron systems (see, for example, review [6]). Therefore, the motivation for PNC experiments in Yb is not testing the Standard Model via a comparison of high-precision theory and experiment, but rather probing low-energy nuclear physics by comparing PNC effects on either a chain of naturally occurring Yb isotopes (^{168}Yb -0.13%, ^{170}Yb -3.04%, ^{171}Yb -14.28%, ^{173}Yb -16.13%, ^{174}Yb -31.83%, ^{176}Yb -12.76%), or in different hyperfine components of the same odd-neutron-number isotope (^{171}Yb -nuclear spin $I = 1/2$ or ^{173}Yb - $I =$

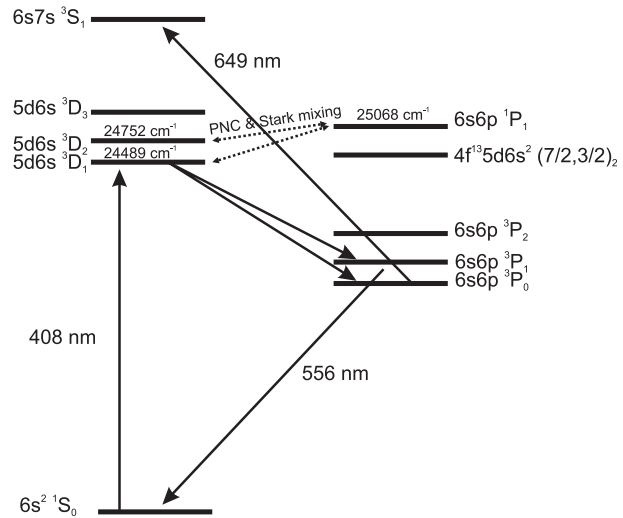


Fig. 1. Low-lying energy eigenstates of Yb and transitions relevant to the PNC experiment.

$5/2$). The former would yield information on the mean-square neutron radii in the chain of isotopes, while the latter would probe nuclear-spin-dependent PNC, which is sensitive to the nuclear *anapole moments* (see, for example, reviews [6,7]) that arise from weak interactions between the nucleons. Both of these types of measurements probe nuclear physics that is exceedingly difficult to ac-

^a Present address: National Institute of Standards and Technology, 325 S. Broadway Boulder, CO 80305-3322

cess by other means, and neither relies on high-precision theory.

2 Preliminary experiments

Experimental work towards an Yb-PNC measurement has started at Berkeley several years ago, and, in its initial phase, was directed towards measurement of various spectroscopic properties of the Yb system of direct relevance to the PNC measurement, including determination of radiative lifetimes [8], measurement of the Stark-induced amplitudes, hyperfine structure, isotope shifts, and dc-Stark shifts of the $6s^2 \ ^1S_0 \rightarrow 5d6s \ ^3D_{1,2}$ transitions, and the quadrupole moment of the latter transition ($\lambda = 404$ nm) [9], and the forbidden magnetic-dipole (M1) amplitude of the former transition ($\lambda = 408$ nm) [10]. For the measurement of the forbidden magnetic-dipole transition amplitude ($\approx 10^{-4} \ \mu_B$), we used the M1-(Stark-induced)E1 interference technique. A simple atomic system where transition amplitudes and interferences are well understood has proven useful for gaining insight into curious Jones dichroism effects that had been studied in condensed-matter systems at extreme conditions and whose origin had been a matter of debate (see Ref. [11] and references therein).

Most recently [12], we reported on an experimental and theoretical study of the dynamic (ac) Stark effect on the $6s^2 \ ^1S_0 \rightarrow 5d6s \ ^3D_1$ forbidden transition. A general framework for parameterizing and describing off-resonant ac-Stark shifts was presented. A model was developed to calculate spectral line shapes resulting from resonant excitation of atoms in an intense standing light-wave in the presence of off-resonant ac-Stark shifts. A bi-product of this work was an independent determination (from the saturation behavior of the 408-nm transition) of the Stark transition polarizability, which was found to be in agreement with our earlier measurement [9].

The present incarnation of the Yb PNC experiment (described below) involves a measurement using an atomic beam. An alternative approach would involve working with a heat-pipe-like vapor cell. Various aspect of such an experiment were investigated, including measurements of collisional perturbations of relevant Yb states [13], nonlinear optical processes in a dense Yb vapor with pulsed UV-laser excitation [14], and an altogether different scheme for measuring PNC via optical rotation on a transition between excited states [15].

3 Experimental technique for the PNC measurement

The general idea of the present Yb-PNC experiment is to excite the forbidden 408-nm transition (Fig. 1) with resonant laser light in the presence of a static electric field. The purpose of the electric field is to provide a reference Stark-induced transition amplitude, much larger than the PNC amplitude. In such a Stark-PNC interference method [16,17], one is measuring the part of the transition probability that is linear in both the reference Stark-induced

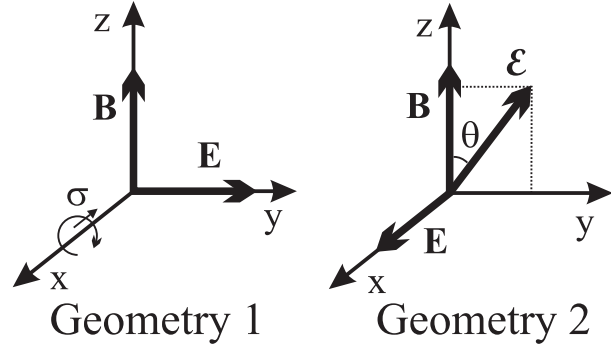


Fig. 2. Possible orientation of fields for PNC-Stark interference experiment. In both cases, light is applied collinearly with x .

amplitude and the PNC amplitude. In addition to enhancing the PNC-dependent signal, employing the Stark-PNC interference technique provides for all-important reversals allowing one to separate the PNC effects from various systematics.

We begin the discussion of the experiment by considering the rotational invariant to which the PNC-Stark-interference term is proportional. Since the effect violates parity and conserves time-reversal invariance, we require the rotational invariant to be P-odd and T-even. The two configurations which have been used for Stark-interference experiments of this type are shown in Fig. 2.

Geometry One was used in the Cs Stark-interference experiment [18] and Geometry Two was used in an early Stark-interference experiment in Tl [19]. The rotational invariant for Geometry One is given by

$$\sigma \cdot (\mathbf{E} \times \mathbf{B}), \quad (1)$$

where σ is the helicity of the excitation light. For Geometry Two, the invariant is

$$(\mathcal{E} \cdot \mathbf{B})([\mathbf{E} \times \mathcal{E}] \cdot \mathbf{B}), \quad (2)$$

where \mathcal{E} is the electric field of the (linearly polarized) light.

The two geometries have very different characteristics and are sensitive to different sets of systematics. Neither geometry is clearly superior. One advantage of Geometry Two is an additional suppression of spurious M1-Stark interference, one of the most important systematic effects in precision PNC-Stark interference experiments. In both Geometries One and Two, this effect can be minimized by the use of a power-build-up cavity to generate a standing light wave. Since a standing wave has no net direction of propagation, \mathbf{k} , any transition rate which is linear in the M1 amplitude (proportional to $\mathbf{k} \times \mathcal{E}$) will cancel out. However, this is the only source of suppression of the M1-Stark interference in Geometry One. This can be seen by replacing σ in the rotational invariant (1) with \mathbf{k} . This is a T-even, P-even rotational invariant which arises from M1-Stark interference. Geometry Two, on the other hand, is such that the M1 and Stark amplitudes are out of phase. Thus, the M1 and Stark amplitudes do not interfere and therefore do not produce additional interference terms

which can change with the changing fields and mimic the PNC-Stark interference. This geometry can even be used in the absence of a power-build-up cavity (and in fact was in the work of Ref. [19]). Thus, the M1-Stark interference term requires a misalignment of the fields along with a net direction of propagation resulting from an imperfect standing wave. This additional reduction of M1-Stark interference has led us to choose Geometry Two for the PNC-Stark experiment.

The rotational invariant (2) highlights some of the salient features of our experiment: the PNC effect reverses with dc electric field (\mathbf{E}), and does not reverse with the magnetic field (\mathbf{B}); however, the presence of the magnetic field is necessary. In fact, the magnetic field should be strong enough so that the transitions to different Zeeman components of the upper state are resolved (because the PNC effect averaged over all Zeeman components is zero). Another reversal is flipping the axis of the light polarization with respect to the E-B plane, which also changes the sign of the PNC effect.

4 PNC signatures for even and odd isotopes

Here we address briefly the effect of the weak mixing between 3D_1 and 1P_1 states on the $6s^2\ ^1S_0 \rightarrow 5d6s\ ^3D_1$ transition. In the present experiment, the forbidden transition rate is enhanced by applying a DC electric field to Yb atoms which mixes the 3D_1 and 1P_1 states. In order to discriminate the weak mixing contribution to the transition rate, a magnetic field is applied leading to Zeeman splitting of the transition into several components. In the case of the Geometry 2 (Fig. 2), for the even ($I = 0$) Yb isotopes, the transition is split onto three components. For the odd isotopes, due to the hyperfine splitting of the 3D_1 state, the magnetic field produces different Zeeman patterns for upper levels with different values of the total angular momentum F' , but in each case, there is an even number of Zeeman components.

A Stark-induced transition amplitude is generally expressed in terms of real scalar (α), vector (β), and tensor (γ) transition polarizabilities [16,9], however, for the case of a $J = 0 \rightarrow J' = 1$ transition, only the vector transition polarizability contributes. The transition amplitude between states with total angular momenta and projections F, M and F', M' takes the form¹

$$A_{FMF'M'}^{Stark} = i\beta_{FF'}(-1)^q (\mathbf{E} \times \boldsymbol{\mathcal{E}})_q \langle F, M, 1, -q | F', M' \rangle, \quad (3)$$

where $q = M - M'$ labels the spherical component and $\langle F, M, 1, -q | F', M' \rangle$ is a Clebsch-Gordan coefficient. The transition amplitude arising due to PNC can be expressed as

$$A_{FMF'M'}^{PNC} = i\xi_{FF'}(-1)^q \boldsymbol{\mathcal{E}}_q \langle F, M, 1, -q | F', M' \rangle. \quad (4)$$

¹ The $(-1)^q$ factor was inadvertently omitted in some of our earlier publications. This has not affected any of the quoted results.

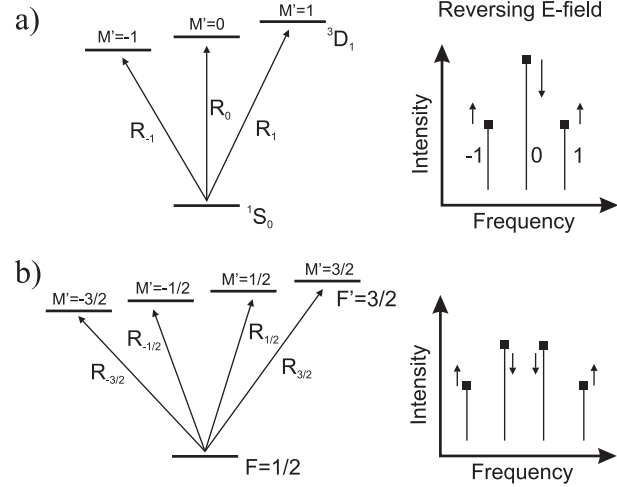


Fig. 3. (a) Level diagram and Zeeman-component spectrum for $^1S_0 \rightarrow ^3D_1$ transition for even Yb isotopes. (b) Same for $^1S_0\ F = 1/2 \rightarrow ^3D_1\ F = 3/2$ for ^{171}Yb . The small arrows indicate the effect of the Stark-PNC interference term – a small relative enhancement of some components and a suppression of others – that reverses with \mathbf{E} and θ .

Here $\xi_{FF'}$ characterizes the PNC-induced electric-dipole transition amplitude.

Assuming that the magnetic field is perpendicular to the electric field and is strong enough to resolve the Zeeman components of the transition, that the light propagates parallel to the electric field, and selecting the quantization axis along the magnetic field, we obtain the following results for the transition rates. For isotopes with zero nuclear spin, the transition rates to Zeeman sublevels $M' = 0, \pm 1$ are:

$$\mathcal{R}_0 = \frac{8\pi}{c} \mathcal{I} [\beta^2 E^2 \sin^2 \theta + 2\xi \beta E \sin \theta \cos \theta], \quad (5)$$

$$\mathcal{R}_{\pm 1} = \frac{4\pi}{c} \mathcal{I} [\beta^2 E^2 \cos^2 \theta - 2\xi \beta E \sin \theta \cos \theta], \quad (6)$$

where \mathcal{I} is the light intensity. In these expressions, we neglect the term in the transition rate which is quadratic in PNC mixing. For an arbitrary angle of the light polarization θ , there are generally three components of the transition as shown in Fig. 3a. Neglecting Stark shifts, the distance between adjacent peaks corresponds to an energy difference

$$\Delta E \approx g\mu_0 M' B, \quad (7)$$

where g is the Landé factor, μ_0 is the Bohr magneton, and B is the magnetic field. The effect of the Stark-PNC interference is to change the relative strength of the two extreme components of the transition with respect to the central component. Expressions (5,6) show explicitly that the PNC effect reverses with both \mathbf{E} and θ .

As an example of a transition for an odd isotope, consider $F = 1/2 \rightarrow F' = 3/2$ of ^{171}Yb (Fig. 3b). Since the magnetic moment of the ground $^1S_0\ F = 1/2$ state is solely due to the nucleus, the Zeeman splitting of this state is three orders of magnitude smaller than that of

the $^3D_1 F = 3/2$ state and is unresolved at the magnetic-field strength of interest. Therefore, the total rates for the transitions to the upper-state Zeeman components M' are sums of the respective rates. The vector transition polarizability $\beta_{FF'}$ is related to that for an isotope with zero nuclear spin (β) according to

$$\beta_{FF'} = \beta(-1)^{I+F} \sqrt{(2F'+1)(2F+1)} \begin{Bmatrix} 1 & F' & I \\ F & 0 & 1 \end{Bmatrix}, \quad (8)$$

where the brackets denote a $6j$ -symbol [20]. The distance between peaks is determined by

$$\Delta E \approx g_{F'} \mu_0 M' B, \quad (9)$$

where $g_{F'}$ is given by

$$g_{F'} = g \cdot \frac{F'(F'+1) + J'(J'+1) - I(I+1)}{2F'(F'+1)}. \quad (10)$$

In calculating the PNC amplitude, one needs to take into account both the nuclear-spin-independent effect (as in the case of the even isotopes), as well as the nuclear spin-dependent contribution, including the effect of the nuclear anapole moment. The PNC signature for this transition is an asymmetry between the two pairs of Zeeman components of the transition (Fig. 3b) which, once again, reverses with \mathbf{E} and θ .

In addition, we note that the $F = 1/2 \rightarrow F' = 1/2$ transition of ^{171}Yb is not influenced by the PNC effect under the discussed conditions. This transition is split by the magnetic field into two Zeeman components, whose intensities must be invariant under the B-field reversal. Thus, the PNC asymmetry cancels. The total rates for these two Zeeman components turn out to be equal and independent of the polarization angle θ . Observation of this transition gives us an additional handle to study systematics.

Using the theoretical value of $\xi \simeq 10^{-9} ea_0$ [2,3] combined with the measured $\beta \simeq 2 \times 10^{-8} ea_0/(\text{V/cm})$ [9,12], we can estimate the relative asymmetry in the line shapes. For example, for \mathcal{R}_0 and $\theta = \pi/4$, and for $E = 1 \text{ kV/cm}$, the asymmetry is $\simeq 10^{-4}$, with the nuclear spin-dependent and isotope-dependent effects expected at a few percent of that (depending on a specific model).

5 Apparatus and signals

A schematic of the Yb-PNC apparatus is shown in Fig. 4. A beam of Yb atoms is produced (inside of a vacuum chamber with a residual pressure of $\approx 5 \times 10^{-6}$ Torr) with an effusive source (not shown), which is a stainless-steel oven loaded with Yb metal. The oven is outfitted with a multi-slit nozzle providing initial collimation of the atomic beam. The oven is operated with the front $\approx 100^\circ\text{C}$ hotter than the rear to avoid clogging of the nozzle. The typical operating temperatures are 500°C in the rear and 600°C in the front. In order to reduce the Doppler width of the 408-nm transition and the overlap between its various

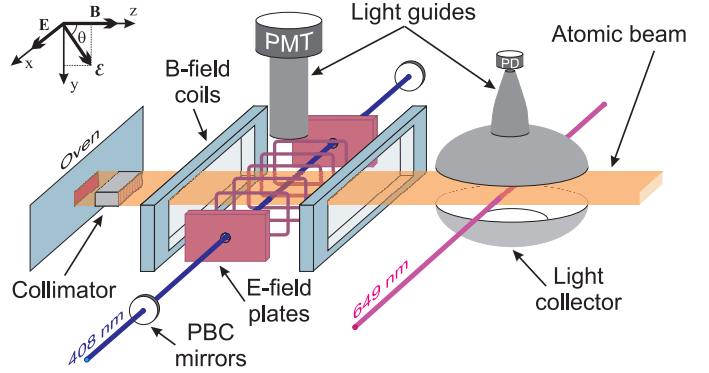


Fig. 4. Schematic of the present Yb-PNC apparatus. Not shown are the atomic-beam oven and the vacuum chamber containing all the depicted elements, except the photomultiplier (PMT), photodiode (PD), and the photodiode light-guide. PBC—power buildup cavity.

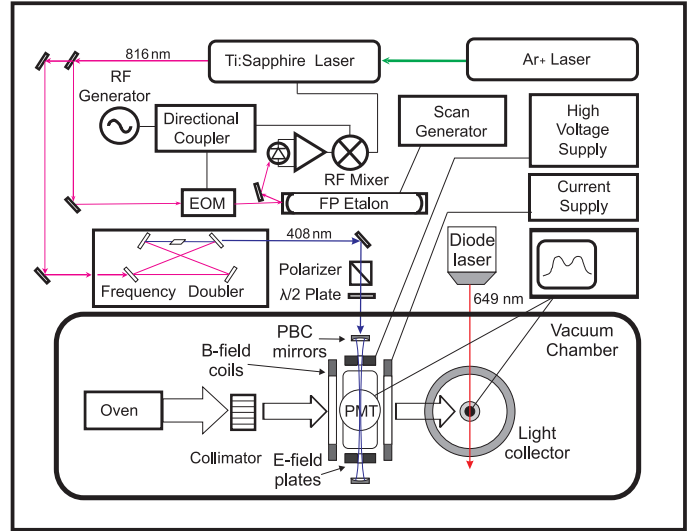


Fig. 5. Schematic of the optical setup and the frequency-locking systems. EOM—electro-optical modulator, FP—Fabry-Perot. The “diode laser” producing 649-nm light consists of a commercial master laser (New Focus Vortex) and a home-made injection-locked diode amplifier.

hyperfine and isotopic components, a downstream external vane collimator was installed. The collimator provides a collimation angle of $\approx 1^\circ$ in the horizontal direction. This reduces the Doppler width of the 408-nm transition to $\approx 12 \text{ MHz}$. The transparency of the collimator is estimated to be $\approx 90\%$. The vane collimator is mounted on a movable platform, allowing precise alignment of its angle relative to the atomic beam during the experiment, as well as its removal from the beam.

Downstream from the collimator, the atoms enter the main interaction region where the Stark- and PNC-induced transition takes place. The light at the transition wavelength of 408.345 nm is produced by doubling the output of a Ti:Sapphire laser (see schematic of the optical arrangement, Fig. 5). A Coherent 899 Ti:Sapphire laser is pumped by $\approx 12 \text{ W}$ from a Spectra Physics 2080 argon-ion

laser operating on all lines. The Ti:Sapphire laser produces ≈ 1.2 W of light at 816 nm. This light is frequency doubled using a commercial bow-tie resonator with a Lithium-Triborate (LBO) crystal (Laser Analytical Systems Wave-train cw). The output of the frequency doubler is ≈ 80 mW.

The 408-nm light is coupled into a power buildup cavity (PBC). We operate the cavity in the confocal regime (mirror radii of curvature and the mirror separation are 25 cm) in order to maintain a relatively large diameter of the light beam by simultaneously exciting many degenerate transverse modes. This is important for our ability to control the ac-Stark shifts without compromising the size of the signals. Precision optical mounts are used for PBC mirrors with micrometer adjustments for the horizontal and vertical angles and the pivot point of the mirror face. The mirrors are attached with RTV adhesive to thin aluminum rings. It was hoped that the thin wall aluminum frame and RTV adhesive would reduce birefringent-induced stress resulting from the adhesion as well as from thermal expansion and contraction. The aluminum frame of one of the mirrors is attached to a piezoelectric ceramic which is attached to the optical mount. The three micrometer adjustments of one of the optical mounts are effected with precision, vacuum compatible pico-motors (New Focus 8302-v) to allow for adjustment of the cavity alignment while in vacuum. The finesse of the PBC was measured using the cavity-ring-down method to be $\mathcal{F} = 4240(70)$. The fraction of the incident light power that could be coupled through the cavity was typically 10-18%, limited to a large extent by the losses in the mirrors (measured at about 240 ppm per bounce). We note that the losses for the mirrors presently used in this experiment are ≈ 40 times larger than those for the mirrors used in some other PBCs (e.g., those in Refs. [18,21]). A reason for such relatively high losses is that our wavelength is significantly shorter. (The losses are expected to be significantly lower in the state-of-the-art mirrors presently on order).

The Coherent 899 Ti:Sapphire laser is rated to have a short-term instability (effective line width) of 500 kHz. In order to reduce the line width of the laser (which is necessary for efficient coupling into the PBC) an electro-optic modulator (EOM) was placed inside the laser cavity. Changing the voltage across the EOM changes the index of refraction of the crystal and therefore the optical-path length. The EOM is capable of extremely fast response with a ≈ 5 MHz bandwidth, limited by the speed of the electronics. The EOM is a double-crystal assembly (LINOS Optics PM 25 IR); the crystals are cut at Brewster's angle to minimize loss and are compensated to prevent walk off of the beam. It is possible to insert the EOM into the cavity and achieve lasing with minimal realignment of the laser. The output of the laser drops $\approx 5 - 10\%$ when the EOM is added. The laser is locked to the PBC using the fm sideband technique [22].

We found that using the PBC as the "master" cavity leads to frequency oscillations at acoustic frequencies. In order to remove these oscillations, the resonant frequency of the cavity is locked to a more stable confocal Fabry-

Perot etalon, once again using the fm sideband locking technique. Thus, the stable (scannable) cavity provides the master frequency, with the power-build-up cavity serving as the secondary master for the laser.

The relative frequency of the laser light is determined using a homemade spherical-mirror Fabry-Perot interferometer operating at 408 nm (not shown in Fig. 5). Since the experiment relies on a detailed understanding of the spectral line shape of the transition over a region of ≈ 100 MHz, a frequency reference with closely spaced frequency markers is needed. To this end, the interferometer is operated with the mirror spacing chosen so that the transverse cavity modes overlap at frequency intervals of $\Delta\nu_{res} = c/(2NL)$, with $N = 7$ (c is the speed of light, and L is the mirror separation) [23]. This allows one to achieve relatively closely spaced frequency markers without making an excessively long cavity. The interferometer consists of two mirrors each of which has a radius of curvature of $R = 50$ cm and the mirrors are separated a distance 38.9 cm. This results in a spacing between the cavity resonances of 55.12 MHz. The cavity is made of invar and placed in an evacuated, passively thermally stabilized enclosure. The frequency drifts of the cavity resonances are ≈ 1 MHz/min.

For the PNC measurements, we plan to take most of the data with an electric-field magnitude in the interaction region of 1.5 kV/cm. The electric field is generated with two copper electrodes with dimensions 4.4x2.5x0.4 cm³ separated by a 6.8-cm gap. In the inter-electrode gap, nine equidistant copper frames are placed for producing a homogeneous voltage drop along the optical axis of the cavity. These frames are connected between each other and the electrodes through 10-M Ω 0.1%-accuracy high-voltage resistors forming a voltage divider. A 10-kV voltage is supplied to the E-field plates by a SPELLMAN CZE1000R power supply modified to allow computer controlled switching of the voltage polarity. During preliminary diagnostic experiments where higher electric field was desirable (see, for example, the data in Figs. 6 and 7), the inter-electrode frames were removed and the gap was reduced to 1 cm. Fields of 12 kV/cm can be reliably obtained without breakdown.

The magnetic field is generated by a pair of rectangular coils having dimensions: 12(width)x3.2(height)x1(depth) cm³ and separated by a 1.4-cm gap. The coils are designed to produce a uniform (1% non-uniformity) axial magnetic field up to 100 G within the region where the atomic beam intersects the waist of the power-buildup cavity (see Fig. 4). The coils are powered by a computer-controlled power supply allowing modulation and reversal of the magnetic field.

Light emitted from the interaction region at 556 nm (Fig. 1) resulting from the second step of the fluorescence cascade following excitation to the 5d6s ³D₁ state is collected with a light guide and detected with a photomultiplier tube. Because of the field requirements in the interaction region, it is difficult to achieve efficient light detection. In order to improve the detection efficiency for the PNC experiment a separate downstream detection region,

dedicated to monitoring the number of atoms making a transition is used. We utilize the fact that 65% of the atoms excited to the $5d6s\ ^3D_1$ state decay to the metastable $6s6p\ ^3P_0$ state (Fig. 1). These atoms are probed by resonantly exciting them (with 649-nm light) out of the $6s6p\ ^3P_0$ state to the $6s7s\ ^3S_1$ state. The subsequent fluorescence is detected in a region free of other experimental components.

The 649-nm light is derived from a single-frequency diode laser (New Focus Vortex) producing ≈ 1.2 mW of cw output that is amplified in home-made injection-locking system to ≈ 7 mW of light sent into the detection region.

The detection region consists of two optically polished curved aluminum reflectors. One reflector, which has hemispherical shape with a radius of curvature of 8.9 cm, covers the upper hemisphere with respect to the intersection of the 649-nm laser beam with the atomic beam. The second reflector is parabolic and is located below the beam intersection. This reflector is positioned in such a way that the focal point of the parabola coincides with the center of curvature of the upper reflector and with the beam intersection. Fluorescent light from the atoms excited with the 649-nm light is collected onto a plastic light guide through a 5-cm diameter opening in the upper reflector. The light-guide is a ‘‘Winston cone’’ [24] designed to efficiently condense the light to the output diameter of the light guide of 1 cm matched to the active area of a silicon photodiode. The use of a photodiode with a higher quantum efficiency than a photomultiplier tube (afforded by larger signals in the detection region) further improves the detection efficiency. We estimate a detection efficiency of $\approx 40\%$ for the atoms in the $6s6p\ ^3P_0$, corresponding to $\approx 26\%$ of the atoms excited to the $5d6s\ ^3D_1$.

Examples of signals obtained with the present apparatus are shown in Figs. 6 and 7.

6 Statistical sensitivity

Based on various parameters achieved in the present apparatus, one can estimate the statistical sensitivity of the PNC experiment. One straightforward way to do it is to note that the Stark-interference technique is a tool for raising the signal above the background and controlling systematic effects. It does not, however, improve the statistical sensitivity for a shot-noise-limited experiment, but merely allows one to achieve the shot-noise limit. Because of this, one can ignore the Stark-interference nature of the experiment in the estimate of the statistical sensitivity of the PNC measurement, and consider instead the statistical sensitivity for direct excitation of the PNC amplitude without any static electric field.

With ≈ 5 W of circulating power in the power-build-up cavity, using a detection efficiency of 26% as discussed above, and a quantum efficiency of the photodiode of $\approx 90\%$, we arrive at the number of detected transitions per second of ≈ 0.7 . Thus, for a shot-noise-limited experiment, the fractional precision is $\delta E_{1\text{PNC}}/E_{1\text{PNC}} \approx 1/\sqrt{\tau(s)}$, where τ is the total integration time of the experiment.

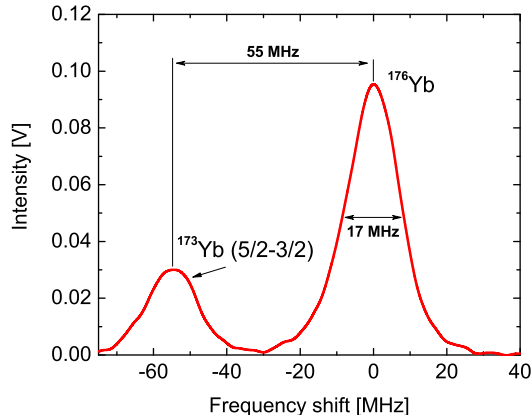


Fig. 6. An example of the 556-nm fluorescence signal detected in the interaction region recorded as the frequency of the 408-nm light was swept across resonances corresponding to two neighboring isotopic hyperfine components of the Stark-induced transition. $E=12$ kV/cm, $B=0$.

A realistic integration time of 10^4 s, gives a fractional precision of $\approx 1\%$.

Achieving this statistical sensitivity seems quite realistic given the current apparatus. A preliminary analysis of systematic effects indicates that systematic errors can be controlled at this level as well. Pushing the precision of the experiment to a level beyond this point will require a significant amount of effort, most notably a dramatic improvement in the power-build-up cavity in order to achieve the necessary statistical sensitivity. While it is difficult to project the ultimate sensitivity of a PNC experiment in Yb, the current status of the experiment gives us reason to hope that a high precision experiment is possible.

7 Analysis of systematics

The current Yb-PNC apparatus has been designed to minimize systematic effects, and the majority of the systematic effects we anticipate will result only in a combination of multiple apparatus imperfections. Several reversals are available (electric and magnetic fields, and light-polarization angle) to control systematics. An additional helpful feature is a specific characteristic light-detuning dependence of the PNC asymmetry.

Our general approach to dealing with systematics is similar to that employed, for example, in Refs. [25, 26]. We begin by making a list of all reasonable apparatus imperfections (field misalignments, inhomogeneities, imperfect reversals, etc.), and write out all possible P,T-even rotational invariants that produce the same signature as the PNC effect upon reversals. We can then artificially impose exaggerated combinations of imperfections in order to measure (and, where possible, minimize) the remaining imperfections. A detailed analysis of the systematics will be given elsewhere. At present, we are confident that

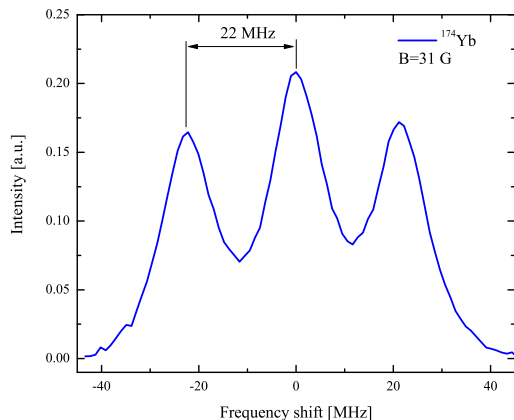


Fig. 7. Same as in Fig. 6, but the scan is over the ^{174}Yb resonance whose Zeeman components are split by an applied magnetic field. The PNC signature is the relative suppression/enhancement of the central peak with respect to the two side peaks that is odd in E and even in B.

initially, systematics should be under control at a $\sim 1\%$ level, sufficient for reliable measurements of the isotopic and hyperfine PNC effects.

8 Conclusions and acknowledgements

We have reported on the progress in the experiment measuring parity-nonconservation effects in ytterbium, which takes advantage of an extraordinary anticipated enhancement of atomic PNC effects (by two orders of magnitude), compared to, for example, Cs. The Yb-PNC experiment relies on proven, although challenging, experimental techniques of atomic physics. The atomic structure of Yb is vastly different from the structure of atoms which have previously been studied in atomic PNC experiments, so the specific features of the experiment are quite different from the earlier work, although there are many features drawn from earlier PNC experiments [19, 4, 25]. The seven stable isotopes of Yb will allow for the first measurement of atomic PNC effects in a chain of isotopes. Assuming the weak-charge variation between the isotopes as predicted by the Standard Model, this will provide a unique way of measuring the variation of neutron r.m.s. radii in an isotopic chain. Conversely, if the neutron radii are known, one can measure the isotopic variation of the nuclear weak charge independent of uncertainties associated with atomic theory. Measurements of the PNC effect on different hyperfine components of the transition of atoms with non-zero nuclear spin nuclei (^{171}Yb and ^{173}Yb) will allow for the first measurements of the nuclear anapole moment in nuclei with unpaired neutrons.

The authors thank A. Dilip, B. P. Das, and M. G. Kozlov for useful discussions. This work has been supported by NSF (Grant 0457086), and by the Director, Office of Science, Office of Basic Energy Sciences, Nuclear Science

Division, of the U.S. Department of Energy under contract DE-AC03-76SF00098.

References

1. D. DeMille, *Physical Review Letters* **74**(21), 4165 (1995)
2. S.G. Porsev, G. Rakhlina Yu, M.G. Kozlov, *JETP Letters* **61**(6), 459 (1995)
3. B.P. Das, *Physical Review A* **56**, 1635 (1997)
4. C.S. Wood, S.C. Bennett, J.L. Roberts, D. Cho, C.E. Wieman, *Canadian Journal of Physics* **77**(1), 7 (1999)
5. J. Guena, M. Lintz, M.A. Bouchiat, *Physical Review A (General Physics)* **71**, 042108 (2005)
6. J.S.M. Ginges, V. Flambaum, *Physics Reports* **397**(2), 63 (2004)
7. W.C. Haxton, C.E. Wieman, in *Annual Review of Nuclear and Particle Science* (2001), Vol. 51, pp. 261–293
8. C.J. Bowers, D. Budker, E.D. Commins, D. DeMille, S.J. Freedman, A.T. Nguyen, S.Q. Shang, M. Zolotarev, *Physical Review A* **53**(5), 3103 (1996)
9. C.J. Bowers, D. Budker, S.J. Freedman, G. Gwinner, J.E. Stalnaker, D. DeMille, *Physical Review A* **59**(5), 3513 (1999)
10. J.E. Stalnaker, D. Budker, D.P. DeMille, S.J. Freedman, V.V. Yashchuk, *Physical Review A* **66**(3), 31403 (2002)
11. D. Budker, J.E. Stalnaker, *Physical Review Letters* **91**(26), 263901/1 (2003)
12. J.E. Stalnaker, D. Budker, S.J. Freedman, J.S. Guzman, S.M. Rochester, V.V. Yashchuk, *Physical Review A* **73**, 043416 (2006)
13. D.F. Kimball, D. Clyde, D. Budker, D. DeMille, S.J. Freedman, S. Rochester, J.E. Stalnaker, M. Zolotarev, *Physical Review A* **60**(2), 1103 (1999)
14. B. DeBoo, D.F. Kimball, C.H. Li, D. Budker, *Journal of the Optical Society of America B-Optical Physics* **18**(5), 639 (2001)
15. D.F. Kimball, *Physical Review A* **63**, 052113 (2001)
16. M.A. Bouchiat, C. Bouchiat, *Journal de Physique I* **36**(6), 493 (1975)
17. R. Conti, P. Bucksbaum, S. Chu, E.D. Commins, L. Hunter, *Physical Review Letters* **42**(6), 343 (1979)
18. C.S. Wood, S.C. Bennett, D. Cho, B.P. Masterson, J.L. Roberts, C.E. Tanner, C.E. Wieman, *Science* **275**(5307), 1759 (1997)
19. P.S. Drell, E.D. Commins, *Physical Review A* **32**, 2196 (1985)
20. I.I. Sobelman, *Atomic Spectra and Radiative Transitions*, Springer Series on Atoms and Plasmas, 2nd edn. (Springer, New York, 1992)
21. C.J. Hood, H.J. Kimble, J. Ye, *Physical Review A* **64**(3), 033804/1 (2001)
22. R.W.P. Drever, J.L. Hall, F.V. Kowalski, J. Hough, G.M. Ford, A.J. Munley, H. Ward, *Applied Physics B-Photophysics and Laser Chemistry* **B31**(2), 97 (1983)
23. D. Budker, S.M. Rochester, V.V. Yashchuk, *Review of Scientific Instruments* **71**(8), 2984 (2000)
24. R. Winston, W.T. Welford, J.C. Miano, P. Bentez, *Non-imaging optics* (Elsevier Academic Press, Amsterdam ; Boston, Mass., 2005)
25. A.T. Nguyen, D. Budker, D. DeMille, M. Zolotarev, *Physical Review A* **56**(5), 3453 (1997)
26. B.C. Regan, E.D. Commins, C.J. Schmidt, D. DeMille, *Physical Review Letters* **88**(7), 071805 (2002)